Modeling and Dynamic Stability Analysis of the Grid-Following Inverter Integrated With Photovoltaics

Surya Prakash, *Graduate Student Member, IEEE*, Omar Al Zaabi, *Member, IEEE*, Ranjan Kumar Behera, *Senior Member, IEEE*, Khaled Al Jaafari, *Senior Member, IEEE*, Khalifa Al Hosani, *Senior Member, IEEE*, and Utkal Ranjan Muduli, *Senior Member, IEEE*

***Abstract*— The power transfer capacity of transmission lines is limited by the stability of the power system. In addition, the dynamics of photovoltaic (PV) integration through the grid-following inverter (GFI) affects the stability limits, which are not well studied in the literature. This article, therefore, focuses on the stability-constrained power transfer capabilities of transmission lines with single-phase PV-GFI integration. An adaptive tuning method is proposed based on the Lyapunov function (LF) analysis that increases the power transfer capability limit. Outer and inner control loop parameters are considered as candidates for the proposed method. The proposed tuning law is not affected by the active and reactive power requirements, low-voltage or overvoltage ride-through, network impedance, and load changes. In addition, an active damping method using a capacitor voltage feedback loop is proposed to eliminate the effect of resonance with improved power quality. The proposed method is validated through simulation and experimental verification for various test scenarios, such as sudden changes in solar irradiance, dynamic load changes, network parameter variation, and grid voltage sag–swell conditions. The proposed tuning method achieves an enhanced power transfer capacity limit compared with the existing method.**

***Index Terms*— Grid-following inverter (GFI), Lyapunov function (LF) analysis, power system stability limit, power transfer capabilities, solar photovoltaic (PV).**

Manuscript received 14 October 2022; revised 27 January 2023 and 30 March 2023; accepted 26 April 2023. Date of publication 3 May 2023; date of current version 2 August 2023. This work was supported in part by the Khalifa University, Abu Dhabi, United Arab Emirates, under Award FSU-2021-006; in part by the Advanced Technology Research Council ASPIRE Virtual Research Institute (VRI) Program, Abu Dhabi, under Award VRI20-07; and in part by the Ministry of Human Resource Development and Ministry of Power, Government of India under IMPRINT Project Sanction Letter under Grant 1-18/2015-TS-TS.I. Recommended for publication by Associate Editor Jonathan W. Kimball. *(Corresponding authors: Utkal Ranjan Muduli; Omar Al Zaabi.)*

Surya Prakash and Ranjan Kumar Behera are with the Department of Electrical Engineering, Indian Institute of Technology Patna, Patna 801103, India (e-mail: suryaprakashele@gmail.com; rkb@iitp.ac.in).

Omar Al Zaabi, Khaled Al Jaafari, Khalifa Al Hosani, and Utkal Ranjan Muduli are with Advanced Power and Energy Center (APEC), Department of Electrical Engineering and Computer Science, Khalifa University of Science and Technology, Abu Dhabi, United Arab Emirates (e-mail: omar.alzaabi@ku.ac.ae; khaled.aljaafari@ku.ac.ae; khalifa.halhosani@ku.ac.ae; utkal.muduli@ku.ac.ae).

Color versions of one or more figures in this article are available at https://doi.org/10.1109/JESTPE.2023.3272822.

Digital Object Identifier 10.1109/JESTPE.2023.3272822

NOMENCLATURE

L_i, r_i	Inverter-side inductor with parasitic resistance.
L_g, r_g	Grid-side inductor with parasitic resistance.
C_f, $C_{\rm dc}$	Filter capacitance and dc-link capacitance.
r_b, L_b	Effective resistance and inductance of BC.
v_g, i_g	Grid voltage and grid current.
$v_{\rm cf}$, $v_{\rm dc}$	Voltage across C_f and dc-link voltage.
i_L, $i_{\rm dcl}$	Load current and loss component of i_g.
$v_{\rm gm}$	Peak magnitude of the grid voltage.
θ_g, ω_g	Grid phase angle and angular frequency.
$f_{{\rm sw}i}$, f_g	Inverter switching frequency and grid frequency.
f_r	Resonance frequency of LCL filter.
$i_{\rm pcc}$	Estimated PCC current.
$v_{\rm pv}$, $i_{\rm pv}$	PV voltage and current.
$p_{\rm pv}$	Solar PV power being supplied.
i_i, i_b	Inverter-side current and BC inductor current.
s_b, s_i	Switching function for BC and GFI.
p_g	Average power injected into the grid.
$\hat{x}_i$, $\tilde{x}_i$	Steady-state and perturbed value of x_i.

I. INTRODUCTION

PHOTOVOLTAIC (PV) systems with integration of the grid-following inverter (GFI) have gained popularity among distributed energy resources in recent decades due to their ease of extension and use in rural areas [1]. Concerns about pollution and noise levels are also driving the government policy to increase PV generation in the electrical grid. However, the intermittent nature of PV systems has an impact on the stability limits of power system transmission networks, as well as power quality [2], further degrading the reliability of the two-stage PV-GFI system. As a result, a strong and decisive controller is required to maintain the stability of the PV-GFI system in the face of changing solar irradiation, load demand, and external disturbances [3].

A two-stage PV power generation system cascades dc–dc boost converter (BC) to the dc-link of GFI. Some literature has investigated the limits of power transfer capability of the GFI-based power systems; however, the stability limits for transmission lines originating from the solar PV-GFI systems have not been well explored. In renewable-source-based energy generation systems, the operation of the GFI

under distortion, transients, fluctuations, harmonics, and dc offsets is more challenging. Therefore, the control design for such PV-GFI systems must meet the criteria of maximum power extraction from input sources, constant dc-link voltage level during linear/nonlinear load operation, and adjustment of the power factor while providing robust and stable dynamic behavior. The control of a PV-GFI system can be divided into two parts: the dc-side control and the ac-side control [4]. The dc-side control implies to the BC, which uses perturb and observe (P&O) [5]-based maximum power point tracking (MPPT) algorithm to extract maximum power from the PV array despite changes in solar irradiation and temperature. To stabilize the maximum power point (MPP) operating point, the proportional–integral (PI) controller is commonly used, but the PI controller often struggles to maintain stability when the operating point drifts away from the MPP [6]. In spite of this, it has various instability issues due to the sampling of the controller and parameter dependency. The fundamental disadvantage of these closed-loop systems is that they do not guarantee global stability when substantial disturbances are introduced. The Lyapunov-function-based control (LFBC) technique improves dynamic performance and ensures global stability during transients. The LFBC technique for BC is used under uncertainty and external disturbances to achieve global stability in a standalone PV system [7]. However, such an LFBC approach can be used for BC systems in grid-connected applications.

Again, the ac-side control performs an inverter switching action to achieve grid synchronization and dc-link voltage control, in addition to satisfying the grid power quality requirements. Two approaches in [8] and [9] are concerned with adjusting the dc-link voltage in response to the changes in grid voltage and minimizing the losses in the GFI. Current harmonics created by ripples in the dc-link and high-frequency switching of the GFI can be decreased in a PV-GFI system using filters L and LCL [10]. Compared with filters L and LC, the LCL filter delivers greater switching harmonic attenuation, less power loss, smaller component size, and lower inverter current ripple. The PI-based current controllers are most effective in the case of three-phase GFI due to their simplicity and the ability to achieve zero steady-state tracking error with a specific operating point [11]. However, complexity in controller tuning gains along with incapacity to deal with periodic disturbances restrict the PI controller to being used in the single-phase GFI system [12], which brings effective usage of the proportional resonant (PR) controller in the single-phase GFI systems. Appropriate damping is essential to eliminate intrinsic resonance in the LCL filter to solve the instability of the power system [13]. A passive damping strategy adds power loss due to additional resistance in the system. When the PR controller approach is used for a GFI system without active damping, the poles are positioned on the imaginary axis of the s-plane. As a result, the grid current suffers frequency oscillation, which could lead to instability in the GFI system. The PR controller uses active damping (a virtual resistor concept) to minimize frequency fluctuation in the grid current, which moves the pole to the left of the s-plane [14]. The performance of the PV-GFI system with a hybrid damping approach is explored in [15], which adds to the complexity of the control algorithm and the power loss. Although the PR used in [16] for a single-phase PV-GFI system has around zero steady-state error, it cannot eliminate the current harmonics that feed into the grid. To avoid control saturation in the existing PR controller, a novel approach is developed in [17], which also achieves accurate current control with low total harmonic distortion (THD) values. An adaptive quasi-PR controller is proposed in [18] for the control of single-phase grid-connected converters operating under multiple perturbations. The grid-integrated PV systems under distorted grid voltage need enhanced grid current harmonic compensation and power ripple mitigation. The control strategy described in [19] includes an advanced proportional multiresonant controller and a compensation for grid voltage sag.

The GFI system, which has its pole on the left side of the s-plane, can be controlled by the LBFC technique without active damping. The LFBC controller provides global stability without active damping. The LBFC with a capacitor voltage feedback approach can enhance the damping ratio by shifting the conjugate poles far away from the imaginary axis. The LFBC can outperform the PR controller due to a larger damping ratio and a quicker transient response. Hence, [20] integrates the LFBC with the PR controller to show good performance for the single-phase grid-connected GFI with fixed dc source. However, the impacts of nonlinear demand and external disturbances caused by PV intermittency are not considered in [20]. Literatures in [21], [22], and [23] assessed the stability analysis of LFBC techniques for the PV-GFI system with L and LC filters. The stability of the PV-GFI system is established in [21] using the Lyapunov function (LF) to achieve robustness against nonideal grid conditions. Since all the phase-locked loops (PLLs) and multiloop controllers have been removed, high dynamic and tracking performance can be further achieved with LFBC. In [24], grid-forming inverters are discussed with transient stability analysis, considering system damping as part of a large-signal analysis. With the aid of an energy-function-based stability assessment, [24] discusses how GFI can cause instability due to loss of synchronism. The stability of PV power generation based on dc-link voltage and reactive power regulation is evaluated in [23], while [25] discusses the stability of PV-GFI with partial shading conditions. It is obvious from [22] and [26] that the PV control parameters have an impact on the transient stability. Increased power transmission capability can result in improved stability by modifying the PV control parameters.

The analysis presented in [27] was insufficient to represent the two-stage control action of the PV-GFI system. Under significant perturbations away from the operating point induced by environmental and load circumstances, this article proposes a controller that can provide a global asymptotically stable performance. The proposed controller can inject the grid current and maintain the global stability of the system without affecting the system dynamics. The proposed control

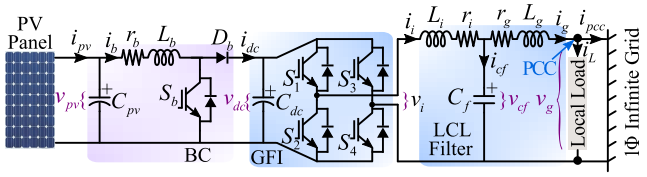

Fig. 1. Two-stage configuration of a single-phase PV-GFI system.

mechanism for the PV-GFI system compensates for nonlinear load requirements while delivering active power from the PV array to the grid. In contrast to the approaches in [28], there is no time delay in acquiring the compensating current reference during a linear/nonlinear load scenario. The current article incorporates the following original contributions.

1) This article discusses the performance analysis of a single-phase PV-GFI system and develops an LFBC strategy while considering the effect of the LCL filter and intermittency of the PV system.
2) The dc-link voltage is a time-varying function that injects dc offset and second-order harmonic ripple content into the grid. The dc-link capacitor $C_{\rm dc}$ is included for analysis to show the intermittency of the PV system in relation to the grid voltage.
3) The proposed LFBC uses a root locus approach to examine closed-loop poles for global stability and active damping to reduce resonance without affecting stability, allowing adaptive tuning of parameters and PLL block using LFs with PV signal measurements to improve power transfer efficiency and performance under solar irradiation and filter parameter variations.

Section II presents the PV-GFI system and its modeling, while Section III explains the LFBC control for GFI and BC with parameter tuning methods for GFI and BC control. Various test situations are discussed in Section IV. The conclusion is drawn in Section V.

II. PV-GFI System Small-Signal Modeling

A. System Description

The two-stage configuration of a single-phase PV-GFI system with the LCL filter is illustrated in Fig. 1. The PV-GFI system is made up of a PV array, a dc–dc BC, and a GFI that is also linked to an LCL filter. The LCL filter is used to reduce the switching harmonics at the ac terminals of the GFI. BC is used to extract power from the PV array at MPP as solar irradiation changes, which involves the first stage of the conversion process. In the second stage of the conversion process, the GFI feeds power into the single-phase grid. The GFI dc-link voltage is adaptive and adjusts the reference voltage based on the voltage variation at the PCC. In addition, the PCC also feeds a mix of linear and nonlinear local loads. By connecting an RL load bank through a diode bridge rectifier, a nonlinear load is emulated.

B. Small-Signal Modeling of GFI

As mentioned, GFI feeds power to the grid through the LCL filter consisting of the capacitor (C_f), inverter-side inductor (L_i), and grid-side inductor (L_g) with internal resistances r_i and r_g, respectively. To design an improved model of a GFI system with PV, the nonlinearity and intermittency of the PV system are taken into account by including the effect of the dc-link capacitor ($C_{\rm dc}$) voltage. The dynamics involved in both the ac and dc sides of GFI can be evaluated using the following equation:

$$\begin{aligned} L_i\frac{di_i}{dt}+r_i i_i &= s_i v_{\rm dc}-v_{\rm cf}, \quad C_f\frac{dv_{\rm cf}}{dt}=i_i-i_g \\ L_g\frac{di_g}{dt}+r_g i_g &= v_{\rm cf}-v_g, \quad C_{\rm dc}\frac{dv_{\rm dc}}{dt}=i_{\rm dc}-s_i i_i \end{aligned} \tag{1}$$

where v_g, $v_{\rm cf}$, and $v_{\rm dc}$ are the measured grid voltage, the voltage across C_f, and dc-link voltage, respectively, through three voltage sensors. i_i and i_L are the inverter-side current and the load current, respectively, and are measured through two current sensors. Let $x_i \in \{v_{\rm dc}, v_{\rm cf}, i_i, i_g, s_i\}$ be the state variables for the GFI small-signal modeling, that is, $x_i = \hat{x}_i + \tilde{x}_i$, where $\hat{x}_i$ and $\tilde{x}_i$ denote its steady-state and perturbed value, respectively. Here, s_i is the GFI switching function. The steady-state value of $\hat{i}_i$, $\hat{v}_{\rm cf}$, and $\hat{s}_i$ can be represented as follows:

$$\begin{aligned} \hat{i}_i &= C_f\frac{d\hat{v}_{\rm cf}}{dt}+\hat{i}_g, \quad \hat{v}_{\rm cf}=L_g\frac{d\hat{i}_g}{dt}+r_g\hat{i}_g+v_g \\ \hat{s}_i &= \frac{1}{\hat{v}_{\rm dc}}\left(L_i\frac{d\hat{i}_i}{dt}+r_i\hat{i}_i+\hat{v}_{\rm cf}\right). \end{aligned} \tag{2}$$

Using an appropriate PLL, the peak magnitude of the grid voltage ($\hat{v}_{\rm gm}$) at PCC can be obtained in the PCC with the phase angle ($\hat{\theta}_g$). For appropriate GFI control, the reference/steady-state value of dc-link voltage ($\hat{v}_{\rm dc}$) must be maintained at $\mu v_{\rm gm}$, i.e., $\hat{v}_{\rm dc} = \mu v_{\rm gm}$. The variable μ is considered as 1.1–1.2 to compensate for the various losses that occur in the operation of the GFI. Moreover, the difference between $v_{\rm dc}$ and $\hat{v}_{\rm dc}$ is fed to a PI regulator with an appropriate limiter to estimate the loss component of the current ($\hat{i}_{\rm dcl}$). $\hat{i}_{\rm dcl}$ further combining with the estimated PCC current ($\hat{i}_{\rm pcc}$) and the load current (i_L) provides the estimated value of the peak grid current $\hat{i}_{\rm gm}$. Multiplying $\sin\hat{\theta}_g$ by $\hat{i}_{\rm gm}$ provides the reference/steady-state value of the grid current $\hat{i}_g$, i.e., $\hat{i}_g = \hat{i}_{\rm gm}\sin\hat{\theta}_g$. The value of dc-link capacitor ($C_{\rm dc}$ limits the GFI lifetime. Hence, a small value of $C_{\rm dc}$ is desired to regulate the ripples in $v_{\rm dc}$ within its reference value of $\hat{v}_{\rm dc}$ and can be expressed as follows:

$$C_{\rm dc} = \frac{P_g}{2\omega_g\hat{v}_{\rm dc}\tilde{v}_{\rm dc}} \tag{3}$$

where ω_g ($= 2\pi f_g$) is the grid angular frequency considering f_g as the grid frequency, and P_g is the average power injected into the grid. Fig. 2(a) indicates the ripple voltage at dc-link for different values of $C_{\rm dc}$. It can be seen that the ripple voltage decreases with increasing dc-link capacitor. However, the large value of $C_{\rm dc}$ leads to an increase in the size, cost, and weight of the GFI with a slower dynamic response.

Taking into account the small-signal model in (1), the averaged linearized state-space model of the GFI system can

be further simplified as follows:

$$\frac{d}{dt}\begin{bmatrix}\tilde{i}_i\\ \tilde{i}_g\\ \tilde{v}_{\rm cf}\\ \tilde{v}_{\rm dc}\end{bmatrix}=\underbrace{\begin{bmatrix}-\tau_i^{-1} & 0 & -L_i^{-1} & \hat{s}_i L_i^{-1}\\ 0 & -\tau_g^{-1} & L_g^{-1} & 0\\ C_f^{-1} & -C_f^{-1} & 0 & 0\\ -\hat{s}_i C_{\rm dc}^{-1} & 0 & 0 & 0\end{bmatrix}}_{A_i}\times\underbrace{\begin{bmatrix}\tilde{i}_i\\ \tilde{i}_g\\ \tilde{v}_{\rm cf}\\ \tilde{v}_{\rm dc}\end{bmatrix}}_{\tilde{x}_i}+\underbrace{\begin{bmatrix}L_i^{-1}\hat{v}_{\rm dc}\\ 0\\ 0\\ -C_{\rm dc}^{-1}\hat{i}_i\end{bmatrix}}_{B_i}\tilde{s}_i \quad (4)$$

where τ_g $(=L_g/r_g)$ and τ_i $(=L_i/r_i)$ represent the grid-side and GFI-side time constant of the LCL filter, respectively. In the PV-GFI system, the design of the LCL filter is essential to attenuate the harmonics and dampen out the filter resonance. The design of L_i is based on the current ripple in i_i at the inverter switching frequency $f_{\rm swi}$, while the design of L_g depends on the attenuation of current harmonics injected into the grid. From Fig. 1, the transfer function $G_i(s)$ can be obtained as (5), where the effect of parasitic r_g and r_i is not considered in the calculation

$$G_i(s)=\frac{i_g(s)}{v_i(s)}=\frac{1}{L_gL_iC_fs^3+(L_g+L_i)s}. \quad (5)$$

The filter is selected based on the methods given in [29] and [30]. Considering the design parameters of Table II, the Bode plot is obtained in Fig. 2(b). The resonance frequency can be selected as 1044.28 Hz according to the calculation given as follows:

$$f_r=\frac{1}{2\pi}\sqrt{\frac{L_i+L_g}{L_iL_gC_f}},\quad 10f_g\le f_r\le 0.5f_{\rm swi} \quad (6)$$

where $f_{\rm swi}$ is considered as the switching frequency of the GFI. The design of the LCL filter is based on the selection of resonance frequency (f_r) and will be selected within the frequency band of the closed-loop system given by (6). Furthermore, Fig. 2(c) depicts the effect of changes in the LCL filter parameters during resonance damping. Increasing LCL filter parameters by 15%, the resonance frequency decreases and causes undesirable oscillations in i_g. However, at 15% lower value of LCL filter, the resonance frequency increases by introducing harmonics into the grid. Hence, it is possible to filter out the high switching frequency component of i_i, while damping out the resonance in grid current i_g using an effective active damping scheme through linearization process mentioned in Fig. 3.

C. Small-Signal Modeling of PV With BC

Fig. 1(left) depicts the circuit diagram of a PV array that supplies solar power $(p_{\rm pv})$ to the dc-link of GFI through a BC. The generated $p_{\rm pv}$ $(=v_{\rm pv}i_{\rm pv})$ needs to be injected into PCC after differencing conversion losses (dc-link loss, switching loss, parasitic resistance losses) and the local load power. The estimated PCC current $(\hat{i}_{\rm pcc})$ injected into the infinite grid can be deduced in terms of $p_{\rm pv}$ and $\hat{v}_{\rm gm}$, i.e., $\hat{i}_{\rm pcc}=2p_{\rm pv}/\hat{v}_{\rm gm}$.

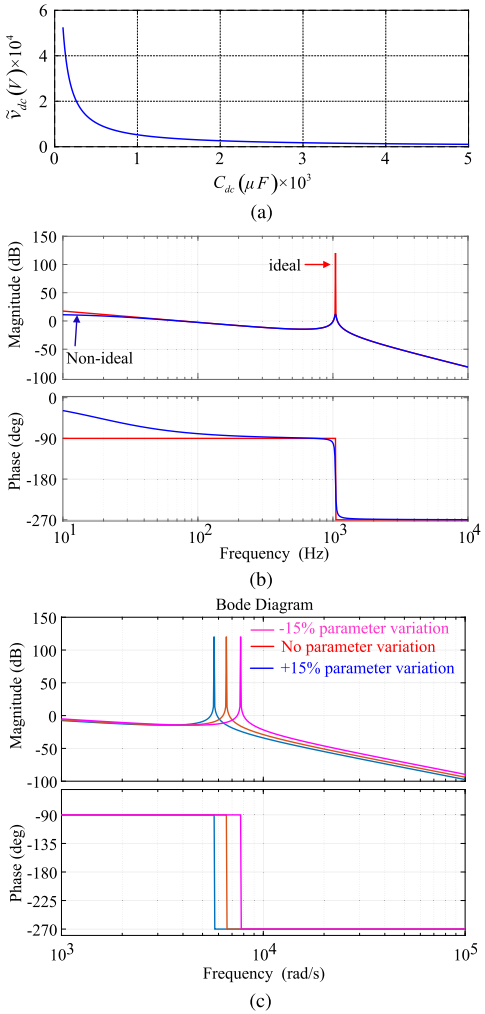

Fig. 2. Time-domain and frequency-domain analyses. (a) Ripple voltage at dc-link for different values of $C_{\rm dc}$. (b) Bode plot of $G_i(s)$ at ideal/no-ideal condition of filter. (c) Bode plot of $G_i(s)$ at change in LCL filter parameter.

The further utilization of $\hat{i}_{\rm pcc}$ is indicated in Section II-B and Fig. 4(a). Furthermore, the purpose of the MPPT control loop for BC is to regulate the inductor current to match the reference PV current generated by the current-oriented MPPT algorithm, as discussed in [31].

The nonlinearity and intermittency of the PV system are considered when designing reformable modeling of the boost system with PV, as follows:

$$\begin{aligned}v_{\rm pv}&=r_bi_b+L_b\frac{di_b}{dt}+(1-s_b)\hat{v}_{\rm dc}\\ C_{\rm pv}\frac{dv_{\rm pv}}{dt}&=i_{\rm pv}-i_b\end{aligned} \quad (7)$$

where r_b and L_b are the resistance and inductance of BC, respectively. The perturbation signals $(\tilde{x_b})$ about the nominal steady-state values $(\hat{x_b})$ are introduced to obtain the BC small-signal model with the variable $x_b\in\{v_{\rm pv}$: PV voltage, $i_{\rm pv}$: PV current, i_b : BC inductor current, and s_b: switching function for BC$\}$, i.e., $x_b=\hat{x}_b+\tilde{x}_b$. By linearizing (7), the average state-space model can be written as follows:

$$\frac{d}{dt}\begin{bmatrix}\tilde{i}_b\\ \tilde{v}_{\rm pv}\end{bmatrix}=\underbrace{\begin{bmatrix}-\tau_b^{-1} & L_b^{-1}\\ -C_{\rm pv}^{-1} & 0\end{bmatrix}}_{A_b}\underbrace{\begin{bmatrix}\tilde{i}_b\\ \tilde{v}_{\rm pv}\end{bmatrix}}_{\tilde{x}_b}+\underbrace{\begin{bmatrix}L_b^{-1}\hat{v}_{\rm dc}\\ 0\end{bmatrix}}_{B_b}\tilde{s}_b \quad (8)$$

where τ_b $(=L_b/r_b)$ is the time constant of the BC. From (7), the steady-state value of the switching function can be obtained as follows:

$$\hat{s}_b = 1 - \left(v_{\rm pv} - i_b r_b\right) \hat{v}_{\rm dc}^{-1}. \tag{9}$$

III. Proposed LF-Based GFI Control

The behavior of the PV-GFI system at its equilibrium point using Lyapunov's stability criteria is studied in this section. This can be accomplished by considering the fact that energy from the PV-GFI system dissipates continuously along its trajectories. Thus, the energy dissipation gradually converges to zero as the system state trajectories approach the equilibrium point. A generalized LFBC methodology is proposed in Section III-A, which can be extended to the GFI and BC, as discussed later in this section.

A. Proposed Control Methodology

A step-by-step description for designing the LFBC methodology using the linearized average state-space model of any switching converter is provided below, and its flowchart is depicted in Fig. 3.

Step 1: Derive the state-space averaged model for the switching converter.

Step 2: Linearize the average state-space model around the steady-state point corresponding to the control target s_j. The small-signal model for the switching converter can be defined as follows:

$$\dot{\tilde{x}}_j = A_j \tilde{x}_j + B_j \tilde{s}_j \tag{10}$$

where $j \in \{b : \text{for BC}, i : \text{for GFI}\}$; A_j and B_j are the system and input matrices, respectively. $\tilde{x}_j$ $(= x_j - \hat{x}_j)$ and $\tilde{s}_j$ $(= s_j - \hat{s}_j)$ represent the state variable and input switching function of the jth converter, respectively.

Step 3: Develop Lyapunov's energy function $E_j(\tilde{x}_j)$ using

$$E_j(\tilde{x}_j) = \frac{1}{2} \tilde{x}_j^T Q_j \tilde{x}_j. \tag{11}$$

Here, $E_j(\tilde{x}_j)$ is considered positive definite, that is, $E_j(\tilde{x}) > 0$, as the matrix Q_j in the following equation is symmetrical and positive definite

$$Q_j = \text{diag}\{L_1, \ldots, L_n, C_1, \ldots, C_n\}. \tag{12}$$

Step 4: Define s_j such that $E_j(\tilde{x}_j)$ must decay over time and can be achieved by taking the time derivative of the energy function $(\dot{E}_j(\tilde{x}_j))$ as follows:

$$\dot{E}_j(\tilde{x}_j) = \underbrace{\frac{1}{2} \tilde{x}^T \left(A_j^T Q_j + Q_j A_j\right) \tilde{x}_j}_{\text{term 1}} + \underbrace{\tilde{x}_j^T Q_j B_j \tilde{s}_j}_{\text{term 2}}. \tag{13}$$

Step 5: Obtain the global stability of the converter system by solving the inequality $\dot{E}_j(\tilde{x}_j) < 0$, i.e., term1 and term2 contribute to a negative value as follows:

$$A_j^T Q_j + Q_j A_j = -P_j \quad \text{and} \quad \tilde{x}_j^T Q_j B_j \tilde{s}_j = -\lambda_j \tag{14}$$

where P_j is a positive semidefinite matrix and can be evaluated using (14). However, the optimal value of λ_j should be selected such that the value λ_j should be a tradeoff between the overshoot and the settling time of the converter system.

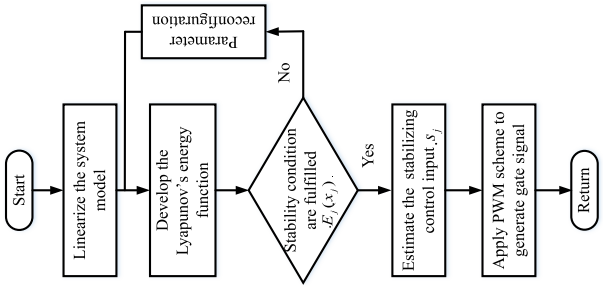

Fig. 3. Proposed control methodology.

Step 6: Evaluate the stabilizing control input variation $\tilde{s}_j$ from the second part of (14) as follows:

$$\tilde{s}_j = -\lambda_j B_j^T Q_j \tilde{x}_j. \tag{15}$$

Step 7: Compute the linearized closed-loop system matrix (A_{cj}) as (16) and find the eigenvalue of A_{cj} for different values of λ_j

$$A_{cj} = A_j - B_j \lambda_j B_j^T Q_j. \tag{16}$$

Step 8: Compute the total stabilizing control input s_j and simulate the nonlinear closed-loop system numerically.

B. Control for GFI With Stability Analysis

The primary goal of controlling the GFI with the LCL filter is to feed clean PV power into the grid. This can be accomplished through an outer voltage loop control and an inner current loop control. The outer loop control generates the reference current to the inner loop controller by regulating the dc-link voltage $v_{\rm dc}$. The inner loop control injects current into the grid so that the grid current i_g should follow the reference current $\hat{i}_g$. In this section, the LFBC method for GFI is used to determine the control input s_i so that the tracking error asymptotically converges to zero. The Lyapunov energy function for the GFI is defined as $E_i(\tilde{x}) = (1/2)\tilde{x}_i^T Q_i \tilde{x}_i$ according to (11). Here, Q_i can be constituted as $Q_i = \text{diag}\{L_i, L_g, C_f, C_{\rm dc}\}$ based on (12).

To achieve the global stability of the GFI, the differentiation of $E_i(\tilde{x}_i)$ should be negative, i.e., $\dot{E}_i(\tilde{x}_i) < 0$. This leads to term1 of $\dot{E}_i(\tilde{x}_i)$ [as in (13)] being negative and yields $A_i^T Q_i + Q_i A_i = -P_i$. The matrix P_i can be obtained as $P_i = \text{diag}\{2r_i, 2r_g, 0, 0\}$ by substituting the matrix of Q_i and A_i from (4) and (12). The matrix P_i is found to be positive semidefinite. Therefore, the stabilizing control input $\tilde{s}_i$ can be effectively calculated as $\tilde{s}_i = -\lambda_i B_i T Q_i \tilde{x}_i$ considering that term2 of $\dot{E}_i(\tilde{x}_i)$ [as in (13)] is negative. Here, the gain λ_i is a positive scalar, i.e., $\lambda_i > 0$. By substituting the matrices Q_i, A_i, and B_i from (4), $\tilde{s}_i$ can be further evaluated as follows:

$$\tilde{s}_i = -\lambda_i \left(\hat{v}_{\rm dc} \tilde{i}_i - \hat{i}_i \tilde{v}_{\rm dc}\right). \tag{17}$$

Equation (17) does not eliminate the damping effect of the resonance. Therefore, (17) provides a globally stable system with a smaller damping factor, as detailed in Section III-D. Equation (17) needs to be modified to improve the damping ratio without compromising global stability. Two cases are

considered to eliminate the resonance effect in the grid current. In case-1, (17) must be adjusted by adding another loop as grid current feedback. Similarly, capacitor voltage feedback is considered as another loop in case-2.

1) Case-1 (Grid Current Feedback Damping): Grid current feedback loop is incorporated into the proposed LFBC approaches in (17) to decrease the grid current oscillation, which is expressed as

$$\tilde{s}_i = -\lambda_i \left(\hat{v}_{\rm dc}\tilde{i}_i - \hat{i}_i\tilde{v}_{\rm dc}\right) - \lambda_g \tilde{i}_g. \tag{18}$$

The switching function of GFI s_i can be obtained by adding (18) and (2), which are represented by

$$s_i = \frac{1}{\hat{v}_{\rm dc}}\left[L_i\frac{d\hat{i}_i}{dt} + r_i\hat{i}_i + \hat{v}_{\rm cf}\right] + \left(-\lambda_i\left(\hat{v}_{\rm dc}\tilde{i}_i - \hat{i}_i\tilde{v}_{\rm dc}\right) - \lambda_g\tilde{i}_g\right). \tag{19}$$

Equation (19) can lower the resonance of a closed-loop single-phase PV-GFI system without compromising its overall stability. The closed-loop state matrix A_{cgi} $(=A_i - B_i\lambda_i B_i^T Q_i)$ can be obtained as (20) using (16)

$$A_{cgi} = \begin{bmatrix} -\left(\lambda_i\hat{v}_{\rm dc}^2 L_i^{-1} + \tau_i^{-1}\right) & -\lambda_g\hat{v}_{\rm dc}L_i^{-1} & -L_i^{-1} & 0 \\ 0 & -\tau_g^{-1} & L_g^{-1} & 0 \\ C_f^{-1} & -C_f^{-1} & 0 & 0 \\ 0 & \lambda_g\hat{i}_i C_{\rm dc}^{-1} & 0 & -\lambda_i\hat{i}_i^2 C_{\rm dc}^{-1} \end{bmatrix}. \tag{20}$$

The stability analysis of the GFI system matrix A_{cgi} may be produced by forming a characteristic equation as

$$\det\left(sI - A_{cgi}\right) = D_{g4}s^4 + D_{g3}s^3 + D_{g2}s^2 + D_{g1}s + D_{g0} \tag{21}$$

where D_{g0}, D_{g1}, D_{g2}, D_{g3}, and D_{g4} are the coefficients of the characteristic equation (21) and can be represented by

$$\begin{aligned} D_{g0} &= \lambda_i\hat{i}_i^2\left(\lambda_i\hat{v}_{\rm dc}^2 + r_g + r_i + \hat{v}_{\rm dc}\lambda_g\right)\Big) \\ D_{g1} &= C_{\rm dc}\left(\lambda_i\hat{v}_{\rm dc}^2 + r_g + r_i + \hat{v}_{\rm dc}\lambda_g\right)\Big) \\ &\quad + \lambda_i\hat{i}_i^2\left(\left(L_i + L_g + C_f r_i r_g + C_f\hat{v}_{\rm dc}^2 r_g\right)\right. \\ D_{g2} &= \lambda_i\hat{i}_i^2 C_f\left(L_i r_g + L_g r_i + L_g\lambda_i^2\hat{v}_{\rm dc}^2\hat{i}_i^2\right) \\ &\quad + C_{\rm dc}\left(L_i + L_g + C_f r_i r_g + C_f\lambda_i r_g\hat{v}_{\rm dc}^2\right) \\ D_{g3} &= C_f\left(C_{\rm dc}L_i r_g + C_{\rm dc}L_g r_i + C_{\rm dc}L_g\lambda_i\hat{v}_{\rm dc}^2 + L_i L_g\lambda_i\hat{i}_i^2\right) \\ D_{g4} &= C_{\rm dc}C_f L_i L_g. \end{aligned} \tag{22}$$

Fig. 5(a) shows a damping ratio performance curve with different values of λ_i and λ_g by analyzing (21). It can be seen that the value of ζ decreases as λ_g increases. Therefore, the proposed LFBC system with grid current feedback is unable to enhance damping. This implies that the grid current feedback damping does not suppress the fluctuation of the grid current, as mentioned in Fig. 6(a).

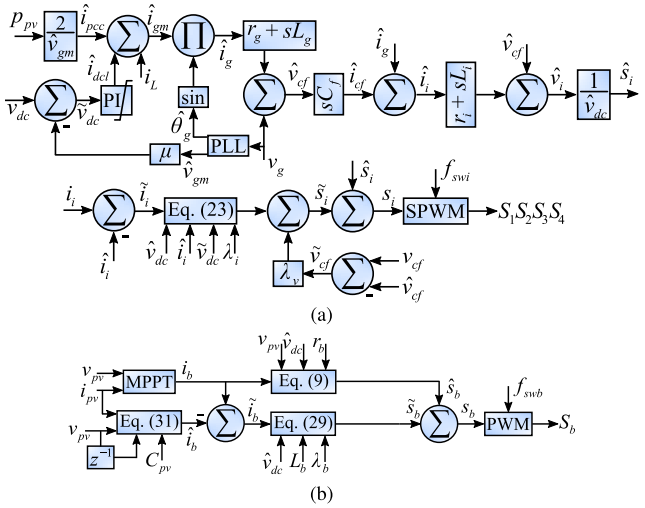

Fig. 4. Proposed Lyapunov control strategy for the two-stage PV-GFI system. (a) GFI pulse generation. (b) BC pulse generation.

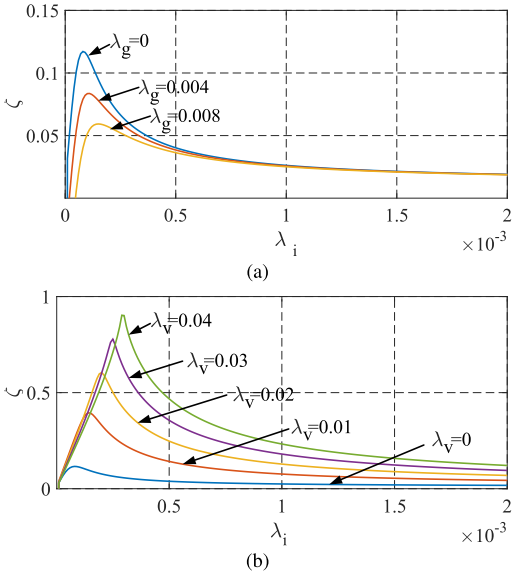

Fig. 5. Effect of damping ratio under variation in λ_i. (a) Different values of λ_g. (b) Different values of λ_v.

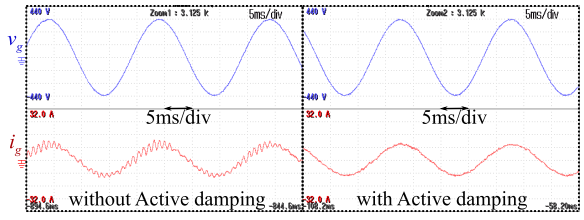

Fig. 6. Experimental result of the single-phase two-stage PV-GFI system for i_g (a) without active damping and (b) with active damping.

2) Case-2 (Capacitor Voltage Damping): In the proposed LFBC, an extra capacitor feedback loop is used in (17) to actively dampen the oscillations of the grid current. Now, (17) can be updated to (23) by including the capacitor voltage error $\tilde{v}_{\rm cf}$

$$\tilde{s}_i = -\lambda_i\left(\hat{v}_{\rm dc}\tilde{i}_i - \hat{i}_i\tilde{v}_{\rm dc}\right) - \lambda_v\tilde{v}_{\rm cf}. \tag{23}$$

With this modification, the proposed control strategy for the PV-GFI inverter is shown in Fig. 4(a). The switching function

of GFI s_i can be expressed using (23) and (2) as follows:

$$s_i = \frac{1}{\hat{v}_{\rm dc}}\left[L_i\frac{d\hat{i}_i}{dt} + r_i\hat{i}_i + \hat{v}_{\rm cf}\right] + \left(-\lambda_i\left(\hat{v}_{\rm dc}\tilde{i}_i - \hat{i}_i\tilde{v}_{\rm dc}\right) - \lambda_v\tilde{v}_{\rm cf}\right). \quad (24)$$

The instantaneous value of s_i is then used for the pulse (S_1, S_2, S_3, S_4) generation through simple sinusoidal pulse width modulation (SPWM) technique, which uses the career frequency of $f_{{\rm sw}i}$. Equation (24) can dampen the resonance without destroying the global stability of the closed-loop single-phase PV-GFI system. The closed-loop state matrix $A_{\rm cvi}$ $(=A_i - B_i\lambda_i B_i^T Q_i)$ can be obtained as (25), as shown at the bottom of the next page, using (16).

Stability analysis of the GFI system matrix $A_{\rm cvi}$ can be obtained through the formation of characteristics as follows:

$$\det(sI - A_{\rm cvi}) = D_{v4}s^4 + D_{v3}s^3 + D_{v2}s^2 + D_{v1}s + D_{v0} \quad (26)$$

where s is an operator in the Laplace domain, and I is the 4×4 identity matrix. The coefficients D_{v0}, D_{v1}, D_{v2}, D_{v3}, and D_{v4} are represented as follows:

$$\begin{aligned}
D_{v0} &= \lambda_i\hat{i}_i^2\left(\lambda_i\hat{v}_{\rm dc}^2 + r_i + r_g + \hat{v}_{\rm dc}\lambda_v r_g\right)\\
D_{v1} &= \lambda_i\hat{i}_i^2\left(C_f r_g\lambda_i\hat{v}_{\rm dc}^2 + L_i + L_g + C_f r_i r_g + \hat{v}_{\rm dc}\lambda_v L_g\right)\\
&\quad + C_{\rm dc}\left(\lambda_i\hat{v}_{\rm dc}^2 + r_i + r_g + \hat{v}_{\rm dc}\lambda_v r_g\right)\\
D_{v2} &= \lambda_i\hat{i}_i^2 C_f\left(L_g\lambda_i\hat{v}_{\rm dc}^2 + L_i r_g + L_g r_i\right)\\
&\quad + C_{\rm dc}\left(C r_g\lambda_i\hat{v}_{\rm dc}^2 + L_i + L_g + C_f r_i r_g + \hat{v}_{\rm dc}\lambda_v L_g\right)\\
D_{v3} &= C_f\left(L_i L_g\lambda_i\hat{i}_i^2 + C_{\rm dc}L_g\lambda_i\hat{v}_{\rm dc}^2 + C_{\rm dc}L_i r_g + C_{\rm dc}L_g r_i\right)\\
D_{v4} &= C_{\rm dc}C_f L_i L_g.
\end{aligned} \quad (27)$$

Fig. 5(b) represents the performance curve between the damping ratio and λ_i with different values of λ_v from (26). It can be seen that increasing λ_v yields the highest ζ. With the proper values of λ_v and λ_i, the oscillation in grid current is reduced, as illustrated in Fig. 6(b). According to the Routh–Hurwitz stability criterion, all the poles are positioned on the left half side of the s-plane if the conditions in the following equation are satisfied

$$A_2A_3 - A_1A_4 > 0 \text{ and } A_1(A_2A_3 - A_1A_4) - A_0A_3^2 > 0. \quad (28)$$

From the known values of the system parameters, the stability of the system can be obtained at $\lambda_i > 0$ and $\lambda_v > 0$.

C. Control of BC With Stability Analysis

An LFBC approach is proposed for BC to track the reference PV current under meteorological conditions. The Lyapunov energy function for BC is defined as $E_b(\tilde{x}_b) = (1/2)\tilde{x}_b^T Q_b\tilde{x}_b$. Here, the matrix Q_b can be restructured as $Q_b = {\rm diag}\{L_b, C_{\rm pv}\}$ using (12). The time derivative of $E_b(\tilde{x}_b)$ should be negative to maintain the global stability of BC, as discussed in Step 4 of the proposed methodology. Now, the condition of term 1 in (14) can be arranged for BC with $A_b^T Q_b + Q_b A_b = -P_b$. The matrix P_b can be obtained as $P_b = -{\rm diag}\{2r_b, 0\}$ by substituting Q_b and A_b from (8). It is observed that P_b is positive semidefinite. Using (15) as a reference, the control input $\tilde{s}_b$ can be effectively derived as $\tilde{s}_b = -\lambda_b B_b^T Q_b\tilde{x}_b$ to stabilize BC behavior. Here, the gain λ_b can be considered as a positive scalar, i.e., $\lambda_b > 0$. The selection of λ_b should be a tradeoff between the overshoot and the settling time of the BC performances. Now, $\tilde{s}_b$ can be derived as (29) by replacing the quantities of (8)

$$\tilde{s}_b = -\lambda_b\hat{v}_{\rm dc}L_b\tilde{i}_b. \quad (29)$$

The desired switching function of BC (s_b) can be expressed as (30) by adding (9) and (29)

$$s_b = \hat{s}_b + \tilde{s}_b = 1 - \left(v_{\rm pv} - i_b r_b\right)\hat{v}_{\rm dc}^{-1} - \lambda_b\hat{v}_{\rm dc}L_b\tilde{i}_b. \quad (30)$$

Using the instantaneous value of s_b, a simple PWM technique is used to generate a pulse (S_b) to drive BC using the triangular career with $f_{{\rm sw}b}$ as the switching frequency. To formulate (30) and track the maximum power from the PV array, LFBC requires one voltage sensor (for $v_{\rm pv}$) and one current sensor (for $i_{\rm pv}$). Instead of using an additional current sensor to detect the inductor current i_b, it can be calculated using the MPPT algorithm, as shown in Fig. 4(b). As a consequence, the cost of the current sensor can be reduced. The estimated reference inductor current $\hat{i}_b$ can be derived from (7) for the kth sampling instant and is given as follows:

$$\hat{i}_b^{(k)} = i_{\rm pv}^{(k)} - C_{\rm pv}T_s^{-1}\left(v_{\rm pv}^{(k)} - v_{\rm pv}^{(k-1)}\right) \quad (31)$$

where T_s is the sampling time of LFBC. The proposed LFBC strategy for BC is shown in Fig. 4(b). The closed-loop state matrix A_{cb} $(=A_b - B_b\lambda_b B_b^T Q_b)$ of BC can be computed as (32) by substituting the matrices Q_b, A_b, and B_b

$$A_{cb} = \begin{bmatrix} -\left(r_b + \lambda_b v_{\rm dc}^2\right)L_b^{-1} & L_b^{-1} \\ C_{\rm pv}^{-1} & 0 \end{bmatrix}. \quad (32)$$

The stability of BC can be evaluated from the characteristic equation of the system matrix A_{cb}, which can be represented as follows:

$$\det(sI - A_{cb}) = s^2 + \underbrace{\left(r_b + \lambda_b v_{\rm dc}^2\right)L_b^{-1}}_{2\zeta_b\omega_b}s + \underbrace{C_{\rm pv}^{-1}L_b^{-1}}_{\omega_b^2} \quad (33)$$

where ζ_b and ω_b represent the damping factor and the natural frequency of LFBC for BC, respectively. I indicates the 2×2 identity matrix. Now, the eigenvalues of the matrix A_{cb} can be represented as follows:

$$s = -\frac{1}{2L_b}\begin{pmatrix} r_b + \lambda_b\hat{v}_{\rm dc}^2 \\ \pm\sqrt{\lambda_b^2\hat{v}_{\rm dc}^4 + 2\lambda_b r_b\hat{v}_{\rm dc}^2 + r_b^2 - 4L_b C_{\rm pv}^{-1}} \end{pmatrix}. \quad (34)$$

The fact that the real part of the eigenvalues in (34) is negative for $\lambda_b > 0$ indicates the stability of the BC system. The damping factor ζ should be $1/\sqrt{2}$ for a fast transient response with less overshoot and a minimum settling time. The value λ_b can be calculated to be 0.000137 $\rm A^{-1}V^{-1}$ by substituting Table I into (33).

TABLE I
PV PANEL RATINGS AND PARAMETERS

Parameter	Value
Open circuit voltage (v_{oc} per panel)	44.14 V
Maximum voltage (v_{pv} per panel)	36.72 V
Short circuit current (i_{sc} per panel)	5.43 A
Maximum current (i_{pv} per panel)	5.03 A
Maximum power (p_{pv} per panel)	184.7 W
Number of series (N_{se}) and parallel panels (N_p)	6 and 3

D. Selection of Controller Gains for GFI

The proper design of the controller gains (λ_i and λ_v) is required to achieve fast dynamic response and global stability of the GFI system. The gains λ_i and λ_v can be selected so that the conjugate poles of the closed-loop system should provide a higher damping ratio. The global stability of the system can be achieved by selecting the optimal value of λ_i and λ_v, which can be obtained from the closed-loop pole at the root locus of the system matrix A_{cvi}.

The effect of the closed-loop pole in (25) is analyzed using the root locus technique with different values of λ_i and λ_v. Fig. 7(a) shows the impact of $\lambda_i \in [0,\ 0.04]$ on the system by considering the gain λ_v as zero. With an increasing value of λ_i, the conjugate poles (p_3 and p_4) shift away from the imaginary axis and increase until the maximum value of the damping ratio reaches 0.116. While p_3 and p_4 move further toward the imaginary axis, the damping ratio decreases. The real poles p_1 and p_2 have also moved away from the imaginary axis. As the highest damping ratio cannot be achieved with the given λ_i, the effect of resonance remains in the system. Fig. 7(b) illustrates the root locus of the conjugate pole with different values of λ_i and λ_v, where λ_i is varied with a different value of λ_v. The real poles are nondominant poles; therefore, it is not considered for analysis in Fig. 7(b). In case the value of λ_v increases, the conjugate pole moves away from the left half of the s-plane and the maximum damping ratio can be achieved with λ_v which eliminates the resonance effect. When $\zeta = 0.707$, the values of λ_i and λ_v are chosen for the optimal transient response. To analyze the global stability of the GFI system in the worst case scenario, a $\pm 15\%$ change in parameters must occur at the same time. The root locus of the closed-loop pole in (25) under parameter variation in L_i, L_g, C, and C_{dc} is shown in Fig. 7(c). The closed-loop poles of A_{cvi} lie on the left side of the s-plane. Thus, the proposed LFBC for the GFI system ensures global stability in the worst case scenario. Fig. 7(d) shows the effect of the damping ratio in (26) under variations in the parameters of the GFI system at constant values of λ_i and λ_v. At $\pm 15\%$ parameter fluctuation in the GFI system, the closed-loop pole of A_{cvi} is directed diagonally upward or downward. Moreover, Fig. 8 demonstrates the relationship between the damping ratio and λ_i under parameter changes in $\pm 15\%$ at constant λ_v. The value of ζ remains nearly constant when the system parameters are changed, and the influence of the transient response is unchanged.

The root locus approach is used to investigate the influence of global stability under the parameter variation in C_{PV} and L_B for the BC system, as shown in Fig. 7(e). For this investigation, the characteristic equation in (33) is used, where $\lambda_b \in [0.000015\ \text{A}^{-1}\text{V}^{-1}, 0.0022\ \text{A}^{-1}\text{V}^{-1}]$ is considered with a parameter variation in $0 \rightarrow \pm 15\%$. It is observed that the system is stable with the placement of poles on the left of the s-plane. Furthermore, Fig. 7(f) illustrates the impact of changing a parameter by a constant value of λ_b on the damping ratios with loci of the poles pointing upward or downward. Consequently, the parameter variations in BC have no significant influence on the damping performance, indicating that the transient performance is unaffected.

IV. RESULTS AND ANALYSIS

A. Prototype Description

The effectiveness and feasibility of the proposed LFBC technique for a single-phase two-stage PV-GFI system are initially verified by the Simulink simulation software. Furthermore, an experimental prototype is developed for such a PV-GFI system, as shown in Fig. 9. The PV-GFI prototype consists of one single-phase GFI, one BC, a PV emulator, a sensor module, a protection circuit, and a dSPACE MicroLabBox-based DSP processor. The single-phase GFI and BC consist of SEMIKRON-made SKM100GB063D IGBT modules, driver boards, and the desired dc-link capacitance. The sensor module has three LEM LA55-P current sensors (to measure i_{pv}, i_i, i_L) and four LEM LV25-P voltage sensors (to measure v_{pv}, v_{dc}, v_{cf}, v_g). A protection circuit consisting of a single-phase contactor is connected at the PCC terminal of the PV-GFI system. The trigger signal for the contactor is generated during undesirable circumstances by the MicroLabBox. As the PV emulator has a rating of 3.5 kW, the components of the entire system are designed accordingly. The parameters used for the respective system are listed in Tables I and II. The sampling frequency of 10 μs is used in MicroLabBox for seamless control with the LFBC implementation.

B. Test Scenarios

The robustness of the proposed LFBC is verified under the four different test scenarios listed below.

1) *Scenario 1:* Sudden change in solar irradiation.
2) *Scenario 2:* 15% variation in LCL filter parameters.
3) *Scenario 3:* Grid voltage sag/swell conditions.
4) *Scenario 4:* System performance under dynamic loads.

$$A_{\text{cvi}} = \begin{bmatrix} -\left(\lambda_i \hat{v}_{\text{dc}}^2 L_i^{-1} + \tau_i^{-1}\right) & 0 & -\left(1+\lambda_v \hat{v}_{\text{dc}}\right) L_i^{-1} & 0 \\ 0 & -\tau_g^{-1} & L_g^{-1} & 0 \\ C_f^{-1} & -C_f^{-1} & 0 & 0 \\ 0 & 0 & \lambda_v \hat{i}_i C_{\text{dc}}^{-1} & -\lambda_i \hat{i}_i^2 C_{\text{dc}}^{-1} \end{bmatrix}. \tag{25}$$

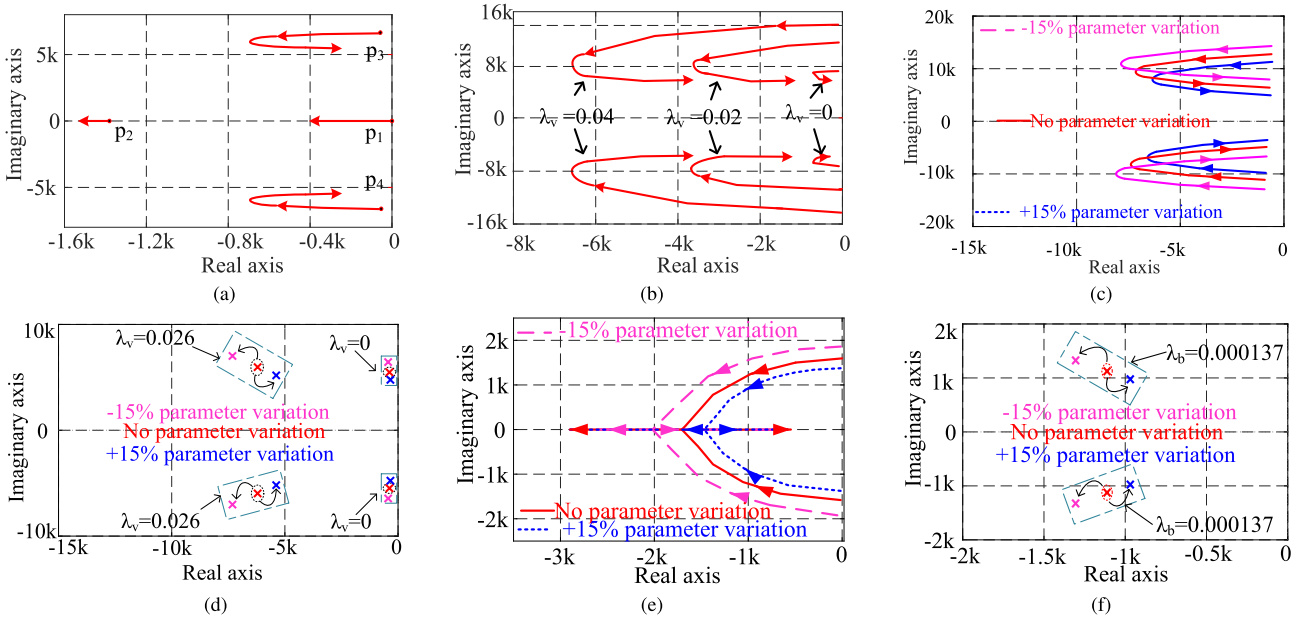

Fig. 7. Root locus for closed-loop poles of A_{cj} ($j \in \{i, b\}$) matrix with different values of λ_i, λ_v, and λ_b. (a) Varying λ_i. (b) Varying λ_i and λ_v. (c) λ_i and λ_v with parameter variation. (d) Parameter variation with varying λ_v. (e) λ_b with parameter variation. (f) Parameter variation with constant λ_b.

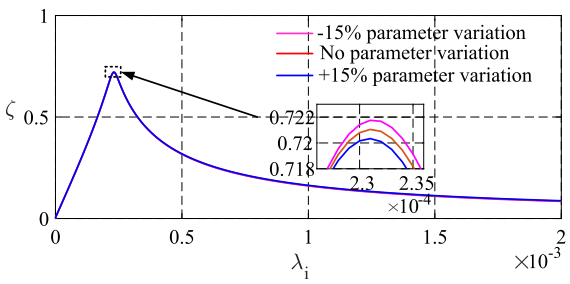

Fig. 8. Effect of damping ratio under change in parameter variation at different values of λ_i at constant λ_v.

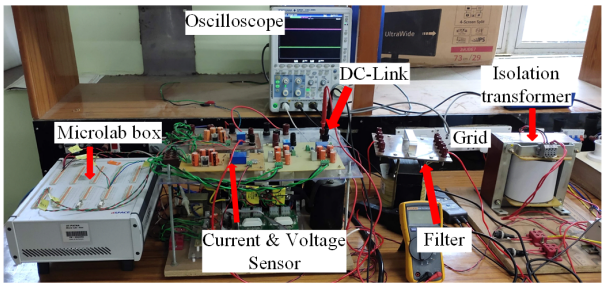

Fig. 9. Laboratory prototype for the proposed system.

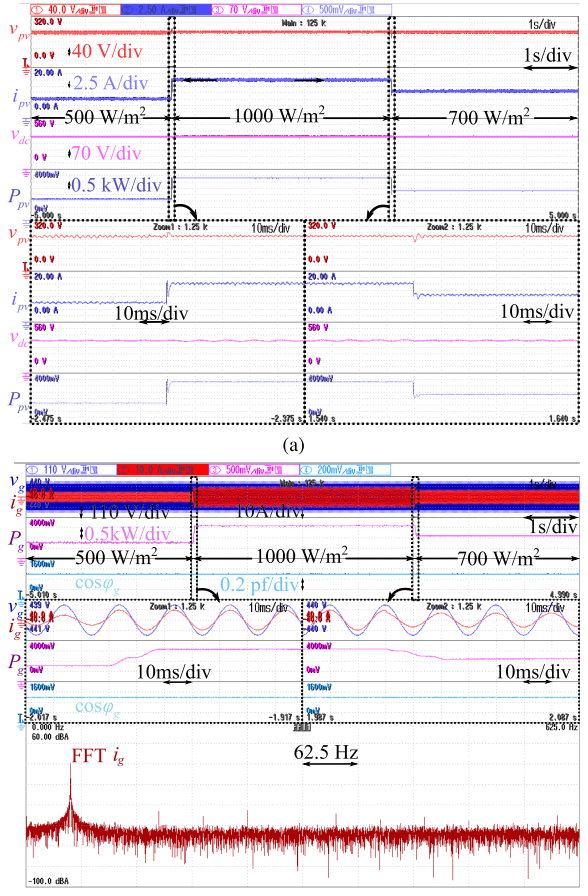

Fig. 10. Experimental results for sudden change in solar irradiation. (a) v_{pv}, i_{pv}, v_{dc} and P_{pv} waveforms. (b) v_g, i_g, P_g and $\cos\phi_g$ waveforms along with FFT of i_g.

These four scenarios appropriately define the various disturbances caused by both PV and the single-phase grid. During these tests, dynamic performances such as v_g, i_g, and p_g are evaluated along with the % THD of i_g to investigate the grid conditions. In addition, the dynamic behavior of v_{pv}, i_{pv}, p_{pv}, and v_{dc} is also evaluated to analyze the PV performance during various test scenarios.

Scenario-1: Fig. 10 illustrates the dynamic performance of a single-phase two-stage PV-GFI system under a sudden change in solar irradiation. It is observed from Fig. 10(a) that the increase or decrease in the PV current i_{pv} depends on the sudden change in solar irradiation. To achieve maximum power, a small change in PV voltage v_{pv} occurs during this scenario. The dc-link voltage v_{dc} adaptively maintains a stable value, considering the effect of BC on the MPPT control. The maximum power of $p_{pv} = 3.32$, 2.315, and 1.62 kW can be drawn from the PV panel during solar irradiation of 1000, 700, and 500 W/m^2, respectively. Subsequently, the PV feedforward term $\hat{i}_{pcc}$ also decreases with a decrease in solar irradiation. As mentioned earlier, the grid current decreases in accordance

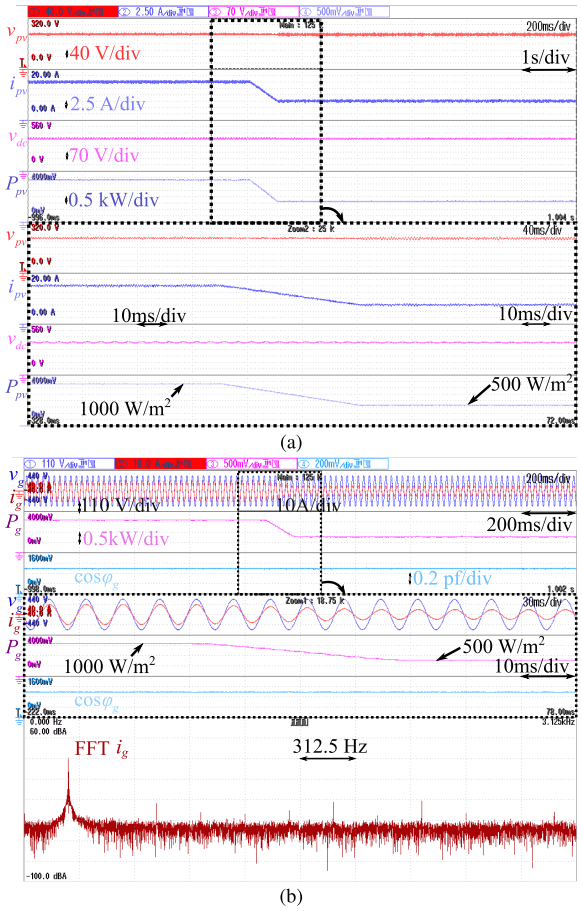

Fig. 11. Experimental results with 15% variation in LCL filter parameters. (a) v_{pv}, i_{pv}, v_{dc} and P_{pv} waveforms. (b) v_g, i_g, P_g and $\cos\phi_g$ waveforms along with FFT of i_g.

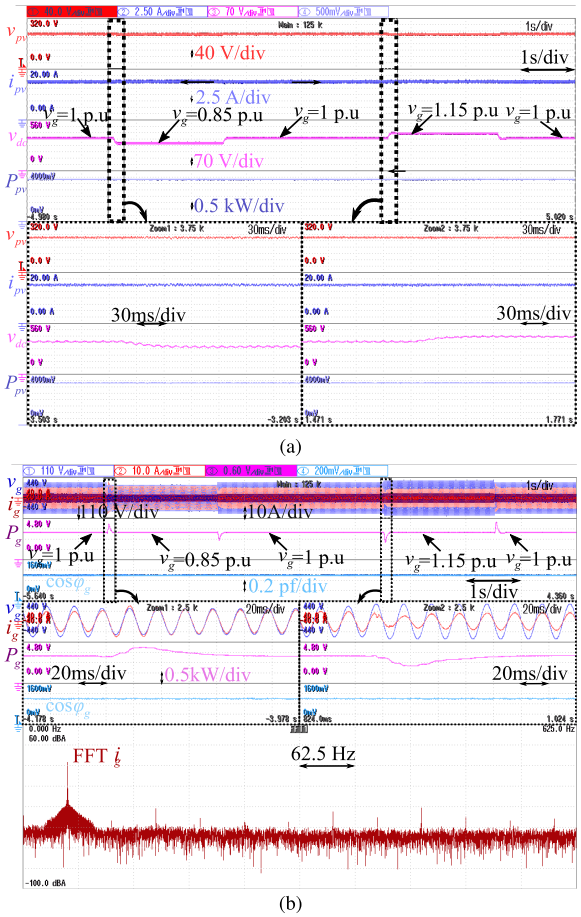

Fig. 12. Experimental results with grid voltage sag/swell conditions. (a) v_{pv}, i_{pv}, v_{dc} and P_{pv} waveforms. (b) v_g, i_g, P_g and $\cos\phi_g$ waveforms along with FFT of i_g.

TABLE II

HARDWARE/SIMULATION PARAMETERS

Parameter	Value
Grid voltage and frequency (v_g, f_g)	230 V, 50 Hz
Boost inductor (L_b)	8 mH
PV capacitor (C_{pv})	50 μF
DC-link capacitor (C_{dc})	2200 μF
Boost switching frequency (f_b)	10 kHz
Inverter switching frequency (f_{sw})	10 kHz
Grid and inverter side inductor (L_i, L_g)	1.436 mH, 0.6867 mH
Filter capacitor (C_f)	50 μF
Internal resistance (r_i, r_g)	0.17 Ω, 0.076 Ω

with the reference generated by the outer loop controller, as depicted in Fig. 10(b). In addition, the injected grid current is also observed to be in phase with the grid voltage. The FFT analysis of i_g for Scenario 1 is shown in Fig. 10(b) (bottom) with a frequency per division of 62.5 Hz. It can be observed that the fundamental peak occurs at 50 Hz, while the third, fifth, and seventh harmonics are less prominent. Therefore, the % THD of i_g at 700 W/m^2 is measured to be $\approx$2.5%. There appears to be an injection of p_g electrical power into the utility grid with a unity power factor. In this scenario, the variation in the injected p_g, which is kept within the IEEE 519-2014 standard limit of 5%, is more noticeable since i_g has a lower % THD.

Scenario-2: In this scenario, the evaluation of the proposed LFBC for a single-phase two-stage PV-GFI system is performed while the estimated parameters differ from the actual parameters by 15%. During this scenario, a linear change in solar irradiation is observed, and the results are verified in Fig. 11. The resilience and reliability of the proposed LFBC are observed in the worst case scenario where all the parameter fluctuations exist simultaneously. Despite these parameter variations, i_{pv} decreases linearly with small variations in v_{pv} during the linear change in solar irradiation from 1000 to 500 W/m^2, as shown in Fig. 11(a). Moreover, the proposed LFBC with the MPPT algorithm tracks the maximum power p_{pv} from the PV panel. The dc-link voltage v_{dc} remains constant during this scenario. In addition, the reference current $\hat{i}_g$ decreases with a reduction in PV power. The proposed LFBC control can dampen out the resonance effect in grid current i_g in the case of parameter variations, as shown in Fig. 11(b). Furthermore, the grid current i_g maintains unity power factor with respect to grid voltage v_g. As a consequence, the proposed controller guarantees stability even in the presence of parameter variations. Fig. 11(b) (bottom) shows an FFT analysis of i_g at 312.5 Hz/div. The fundamental peak is observed at fundamental frequency, and low-order harmonics have significantly less effect under Scenario 2. The % THD is determined to be 1.5% at 1000 W/m^2, which is substantially below the IEEE 519-2014 standard limit of 5%.

Scenario-3: The dynamic performance of the proposed controller under sag/swell of the grid voltage is shown in Fig. 12. During this scenario, the PV panel is operated at constant irradiation and temperature that maintains v_{pv}, i_{pv},

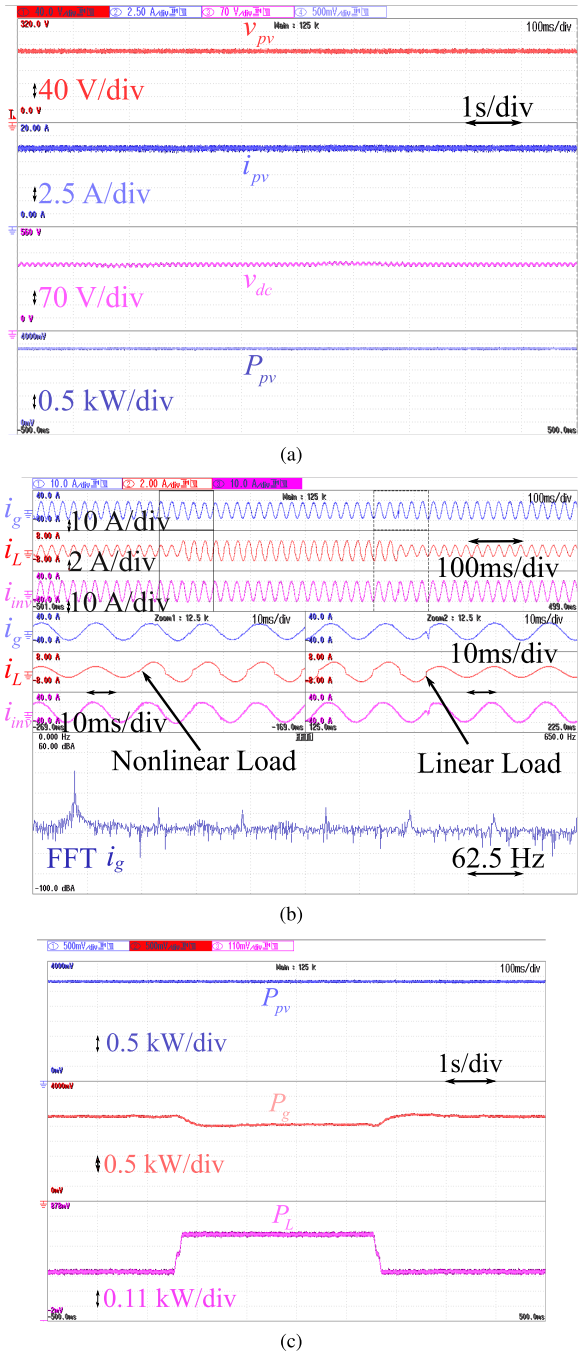

Fig. 13. Experimental results of system performance under dynamic loads. (a) $v_{\rm pv}$, $i_{\rm pv}$, $v_{\rm dc}$ and $P_{\rm pv}$ waveforms. (b) i_g, i_L and i_{inv} waveforms along with FFT of i_g. (c) $P_{\rm pv}$, P_g and P_L waveforms.

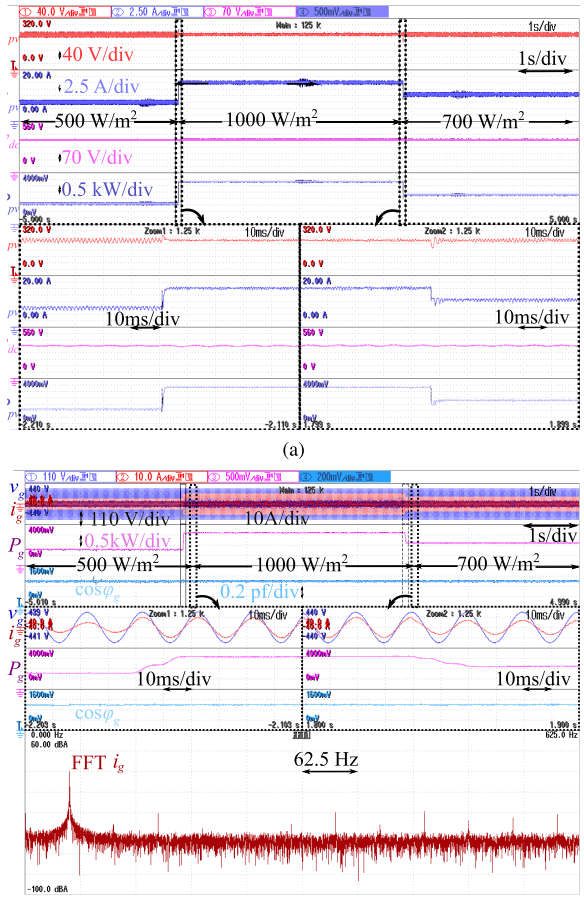

Fig. 14. Comparative experimental results for a sudden change in solar irradiation using [33]. (a) $v_{\rm pv}$, $i_{\rm pv}$, $v_{\rm dc}$ and $P_{\rm pv}$ waveforms from top to bottom. (b) v_g, i_g, P_g and $\cos\phi_g$ waveforms along with FFT of i_g.

and $p_{\rm pv}$ to its rated value, as shown in Fig. 12(a). The maximum amplitude of v_g is used to estimate the reference $\hat{v}_{\rm dc}$ using a loss factor μ. Hence, the adaptive $v_{\rm dc}$ decreases during the sag condition and increases in the swell condition of v_g, as seen in Fig. 12(a). Since LFBC operates in constant power mode, the reference grid current $\hat{i}_g$ increases as v_g decreases or vice versa. The proposed LFBC has the ability to track the reference current efficiently and also inject the grid current into the grid. Fig. 12(b) shows an increase in i_g in a voltage sag scenario. When v_g is restored from 195 to 230 V, i_g maintains the previous value. When v_g increases from 230 to 265 during the swell condition, the grid current i_g decreases further. Fig. 12(b) illustrates injection of p_g into the grid at almost unity power factor. Fig. 12(b) (bottom) indicates the FFT analysis of i_g at 62.5 Hz/div under the 0.15 p.u. voltage sag that occurs in grid voltage. In Scenario 3, the % THD of i_g is approximated to 3.4% with the proposed LFBC technique. The proposed control approach maintains % THD of i_g below 5% according to the IEEE 519-2014 standard under voltage sag/swelling condition.

Scenario-4: The dynamic performance of a single-phase two-stage PV-GFI system under load perturbations at constant solar irradiation is shown in Fig. 13. A diode bridge rectifier with the RL load is considered as a nonlinear load for this case. It can be observed from Fig. 13(a) that $v_{\rm pv}$, $i_{\rm pv}$, and $p_{\rm pv}$ remain in the rated value of the PV panel during load perturbations. Fig. 13(b) depicts the performance of i_i, i_L, and the injected current during linear and nonlinear load conditions. It can be observed that i_i acts as a harmonic compensator for the nonlinear load. Moreover, the proposed LFBC ensures injection of sinusoidal current, thereby minimizing harmonics. Thus, the GFI acts as a harmonics compensator and injects the active power generated from the PV array into the grid. The power flow of a PV-GFI system is shown in Fig. 13(c). It shows the power flow between the PV, local load, and the grid. It can be concluded that PV power maintains its rated value of 3.32 kW while the load fluctuates. The injected power is the sum of the PV and load power vectors, considering the additional losses in the PV-GFI system. When the load demand

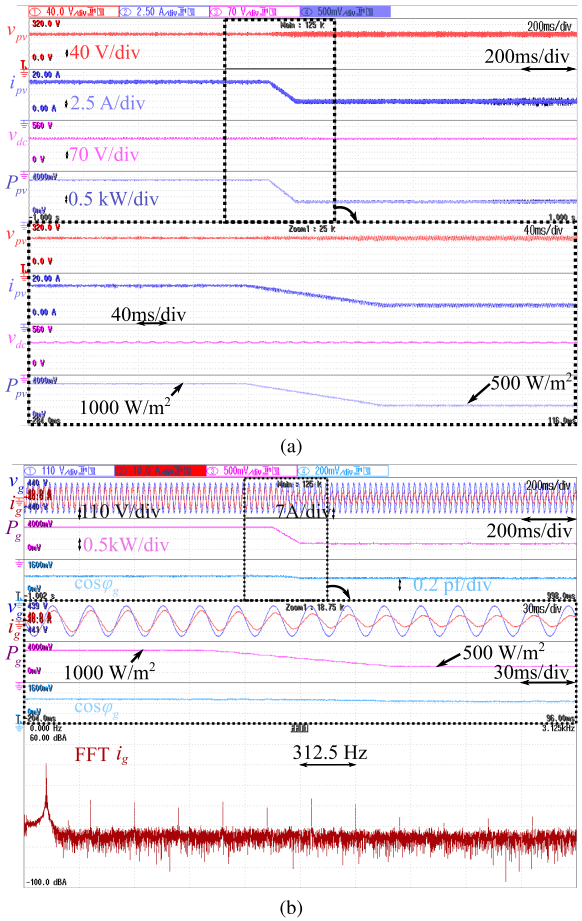

Fig. 15. Comparative experimental results with 15% variation in LCL filter parameters using [33]. (a) v_{pv}, i_{pv}, v_{dc} and P_{pv} waveforms. (b) v_g, i_g, P_g and $\cos\phi_g$ waveforms along with FFT of i_g.

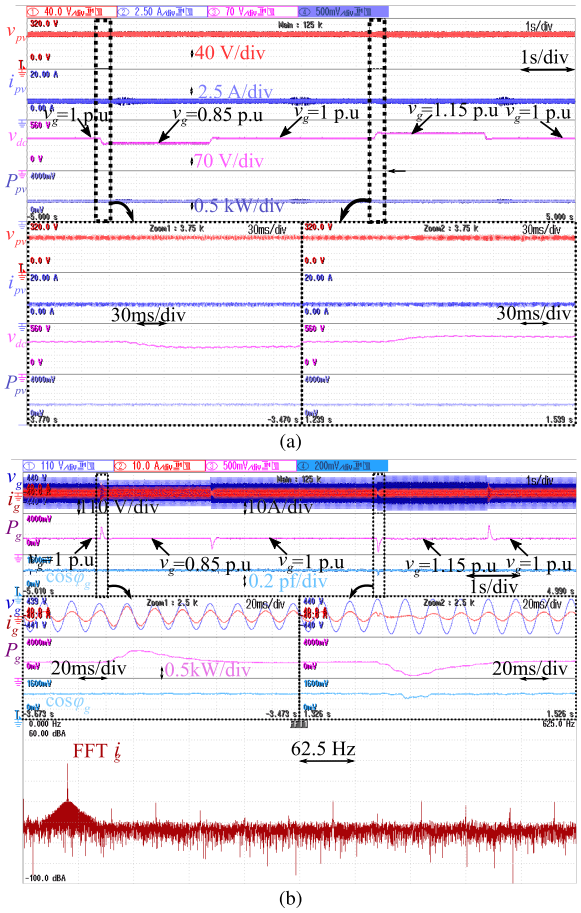

Fig. 16. Comparative experimental results with grid voltage sag/swell conditions using [33]. (a) v_{pv}, i_{pv}, v_{dc} and P_{pv} waveforms. (b) v_g, i_g, P_g and $\cos\phi_g$ waveforms along with FFT of i_g.

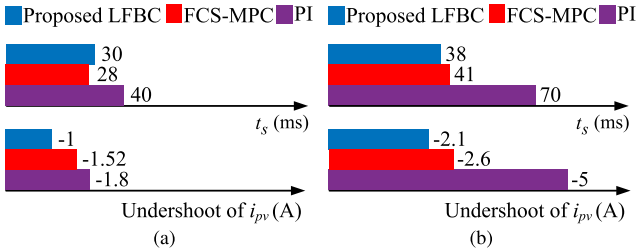

Fig. 17. Performance assessment of the BC system with different controllers. (a) Change in solar irradiation. (b) Change in solar temperature.

increases, the active power injected into the grid decreases. The observed % THD of i_g is 2.3%, as shown in Fig. 13(b). The proposed controller can maintain a sinusoidal grid current without distortion even when the nonlinear load is connected or disconnected.

C. Comparative Performance

Figs. 14–16 show the comparative performance evaluation of the GFI system using the finite-control-set model predictive control (FCS-MPC) [33] technique. The proposed method has less undershoot in i_{pv} compared with the FCS-MPC method in PV voltage, as shown in Fig. 14(a). At the bottom of Fig. 14(b), the FFT analysis of i_g is presented at a frequency per division of 62.5 Hz/div. In Scenario 1, the fundamental peak is at 50 Hz, and the low-order harmonics are less evident. The % THD of i_g is 4.5% corresponding to solar irradiance of 700 W/m^2. Similarly, the % THD of i_g can be achieved as 7.5% at 500 W/m^2 and 4.43% at 0.15 voltage sag under scenarios 2 and 3, respectively, as shown in Figs. 16(b) (bottom) and 15(b) (bottom). Small peaks at low-order harmonics are seen in the FFT analysis of Fig. 15(b) (bottom) during parameter variation, indicating that the FCS-MPC approach is totally parameter-dependent. From a similar comparative study in Figs. 16 and 15 for scenarios 2 and 3, it can be concluded that the proposed LFBC technique has a better % THD response than the FCS-MPC [33] technique. In addition, the performances of the FCS-MPC method have less accuracy under parameter variation, since this method is completely parameter-dependent.

The proposed LFBC along with the FCS-MPC [33] and PI [5] controller is used for the dynamic study of BC during the change in solar irradiance and solar temperature. The performance evaluation of the undershoot and settling time t_s of i_{pv} at the stochastic PV system behavior is shown in Fig. 17. During the simulation study, identical operating circumstances are maintained with the same rating of the PV-GFI system. The proposed LBFC approach has less undershoot in i_{pv} than the existing methods, with a setting time of 30 ms under the change in solar irradiance. Compared with the FCS-MPC and PI methods under change in temperature, the proposed LBFC technique has a fast settling time and a minimum undershoot in i_{pv}. The assessment of % THD of i_g is performed for the GFI

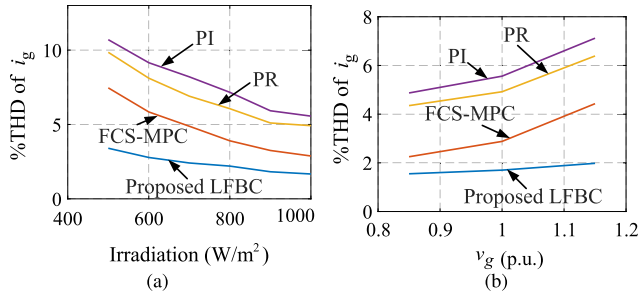

Fig. 18. % THD curve for different current controller techniques' single-phase GFI system. (a) Change in solar irradiation. (b) Change in grid voltage.

system during the change in solar irradiance and the change in the grid voltage. This comparative evaluation is done for inner-loop current controllers such as the proposed LFBC, FCS-MPC [33], PR [14], and PI [14] controller, as shown in Fig. 18. Comparative performance evaluation for the GFI system is made using the FCS-MPC controller [33], PR [14], PI [14], and the proposed methods. Fig. 18(a) and (b) shows the % THD of i_g with the change in irradiance and grid voltage, respectively. The comparative study validates the superiority of the proposed LFBC over the existing control strategies FCS-MPC, PR, and PI method. Furthermore, the proposed LBFC approach keeps the % THD of i_g within the IEEE 519-2014 limit and lowers the % THD when there is a change in irradiance and grid voltage.

Incorporating the grid-integrated rooftop PV system, Table III shows comparison of the proposed LFBC methodology with the existing methods [14], [17], [18], [25], [33]. Compared with the existing methods, the proposed technique shows good performance even when the system parameters vary. However, FCS-MPC has limited accuracy under parameter uncertainty and unknown disturbances. The proposed techniques have inherent load rejection capability, which eliminates the need for an additional filter. The linear controller [14], [17], [18] can ensure local stability at a specific operating point. However, it cannot guarantee stable operation in all the situations caused by significant changes in the operating point. The proposed LBFC approaches allow for a quick dynamic response and guarantee the global stability of the closed-loop system.

D. Performance Analysis of the Proposed Controller in Three-Phase System

To evaluate the performance of the proposed control techniques, the GFI system used specific parameters, including inverter-side resistance per phase of 0.17 Ω, grid-side resistance per phase of 0.076 Ω, inverter-side inductor per phase of 1.436 mH, grid-side inductor per phase of 0.6867 mH, filter capacitor per phase of 50 μF, and grid phase voltage (v_g^a) of 110 V. The parameters for the PV array are also used, as specified in Table I, with the number of series and parallel panels being $N_{\text{se}} = 6$ and $N_p = 1$, respectively.

The effectiveness of the proposed control techniques for the three-phase two-stage PV-GFI system under changes in the irradiance of the PV array is shown in Fig. 19. A sudden variation in solar irradiation can cause a change in

TABLE III
COMPARATIVE STUDY OF THE PROPOSED AND EXISTING METHODS

Control method	Proposed method	FCS-MPC [33]	Passivity-based control [25]	PR with anti windup [17]	PR control [14]	AQ-PR [18]	PI control [14]
Design rule	PP	CF	NR	NR	BP	NR	BP
Computation Burden (μs)	22.6	45.23	26.57	31.2	23.5	24.5	18.3
Switching Frequency	Fixed	Variable	Fixed	Fixed	Fixed	Fixed	Fixed
Additional Filter of i_L	No	NR	Yes	NR	NR	NR	NR
Parameter Variation Effect	Least	NR	NR	NR	More	NR	NR
Global stability	Yes	No	Yes	No	No	No	No
Type of filter	LCL	LCL	L	L	LCL	L	LCL
Type of damping	Active	Active	NA	NA	Active	NA	Active
Dynamic response	Better	Best	Best	Fair	Fair	Fair	Fair
% THD i_g	1.5	2.88	2.2	3.6	4.92	3.92	5.56

Note: NR: Not reported; NA: Not Applicable; PP: Pole Placement; CF: Cost Function; BP: Bode Plot

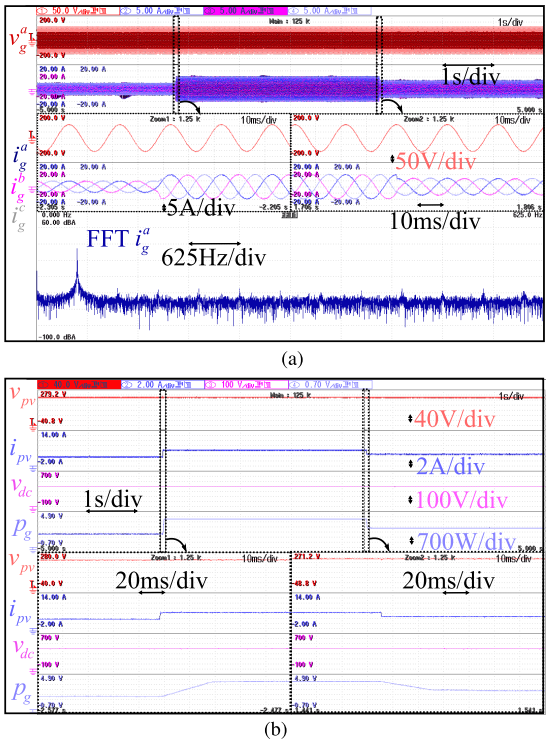

Fig. 19. Dynamic performance of the proposed LBFC controller for a three-phase PV-GFI system under change in solar irradiance. (a) v_g^a, i_g^a, i_g^b, and i_g^c. (b) v_{pv}, i_{pv}, v_{dc}, and p_g.

the PV current (i_{pv}), as depicted in Fig. 19(b). To achieve maximum power output, a corresponding slight variation in PV voltage (v_{pv}) occurs. In addition, the dc-link voltage (v_{dc}) remains constant during this event. In accordance with the reference generated by the outer loop controller, the grid current decreases, as shown in Fig. 19(a). As a consequence, a reduction in injected power (p_g) occurs with a decrease in solar irradiation. In this situation, the grid phase voltage (v_g^a) and grid phase current (i_g^a) are maintained at unity power

factor. In this scenario, it is observed that i_g^a exhibits a THD of less than 5% and retains a sinusoidal waveform.

V. Conclusion

The LFBC controller design and robust performance have been validated through an experimental prototype for a 3.3-kW single-phase PV-GFI system with an LCL filter. The controller uses an adaptive control method with decreasing error accumulation for PI parameter tuning, which increases the power transfer capability under stability constraints. The proposed LFBC controller guarantees global stability and has substantial resonance damping to improve power quality, making it suitable for applications such as rooftop and water pumping systems.

References

[1] R. Panigrahi, S. K. Mishra, S. C. Srivastava, A. K. Srivastava, and N. N. Schulz, "Grid integration of small-scale photovoltaic systems in secondary distribution network—A review," *IEEE Trans. Ind. Appl.*, vol. 56, no. 3, pp. 3178–3195, May 2020.

[2] N. E. Zakzouk, A. K. Abdelsalam, A. A. Helal, and B. W. Williams, "PV single-phase grid-connected converter: DC-link voltage sensorless prospective," *IEEE J. Emerg. Sel. Topics Power Electron.*, vol. 5, no. 1, pp. 526–546, Mar. 2017.

[3] R. A. Mastromauro, M. Liserre, and A. Dell'Aquila, "Control issues in single-stage photovoltaic systems: MPPT, current and voltage control," *IEEE Trans. Ind. Informat.*, vol. 8, no. 2, pp. 241–254, May 2012.

[4] S. B. Kjaer, J. K. Pederson, and F. Blaabjerg, "A review of single-phase grid-connected inverters for photovoltaic modules," *IEEE Trans. Ind. Appl.*, vol. 41, no. 5, pp. 1292–1306, Sep./Oct. 2005.

[5] A. Sangwongwanich, Y. Yang, and F. Blaabjerg, "High-performance constant power generation in grid-connected PV systems," *IEEE Trans. Power Electron.*, vol. 31, no. 3, pp. 1822–1825, Mar. 2016.

[6] N. Femia, G. Petrone, G. Spagnuolo, and M. Vitelli, "A technique for improving P&O MPPT performances of double-stage grid-connected photovoltaic systems," *IEEE Trans. Ind. Electron.*, vol. 56, no. 11, pp. 4473–4482, Nov. 2009.

[7] A. Hussain, M. M. Garg, M. P. Korukonda, S. Hasan, and L. Behera, "A parameter estimation based MPPT method for a PV system using Lyapunov control scheme," *IEEE Trans. Sustain. Energy*, vol. 10, no. 4, pp. 2123–2132, Oct. 2019.

[8] S. Pradhan, B. Singh, and B. K. Panigrahi, "A digital disturbance estimator (DDE) for multiobjective grid connected solar PV based distributed generating system," *IEEE Trans. Ind. Appl.*, vol. 54, no. 5, pp. 5318–5330, Sep. 2018.

[9] J. M. S. Callegari, A. F. Cupertino, V. D. N. Ferreira, and H. A. Pereira, "Minimum DC-link voltage control for efficiency and reliability improvement in PV inverters," *IEEE Trans. Power Electron.*, vol. 36, no. 5, pp. 5512–5520, May 2021.

[10] M. G. Taul, X. Wang, P. Davari, and F. Blaabjerg, "An overview of assessment methods for synchronization stability of grid-connected converters under severe symmetrical grid faults," *IEEE Trans. Power Electron.*, vol. 34, no. 10, pp. 9655–9670, Oct. 2019.

[11] A. Timbus, M. Liserre, R. Teodorescu, P. Rodriguez, and F. Blaabjerg, "Evaluation of current controllers for distributed power generation systems," *IEEE Trans. Power Electron.*, vol. 24, no. 3, pp. 654–664, Mar. 2009.

[12] Y. Yang, K. Zhou, and F. Blaabjerg, "Current harmonics from single-phase grid-connected inverters-examination and suppression," *IEEE J. Emerg. Sel. Topics Power Electron.*, vol. 4, no. 1, pp. 221–233, Mar. 2016.

[13] A. B. Nassif, W. Xu, and W. Freitas, "An investigation on the selection of filter topologies for passive filter applications," *IEEE Trans. Power Del.*, vol. 24, no. 3, pp. 1710–1718, Jul. 2009.

[14] C. Bao, X. Ruan, X. Wang, W. Li, D. Pan, and K. Weng, "Step-by-step controller design for LCL-type grid-connected inverter with capacitor–current-feedback active-damping," *IEEE Trans. Power Electron.*, vol. 29, no. 3, pp. 1239–1253, Mar. 2014.

[15] Y. Lei, W. Xu, C. Mu, Z. Zhao, H. Li, and Z. Li, "New hybrid damping strategy for grid-connected photovoltaic inverter with LCL filter," *IEEE Trans. Appl. Supercond.*, vol. 24, no. 5, pp. 1–8, Oct. 2014.

[16] M. Castilla, J. Miret, J. Matas, L. Garcia de Vicuna, and J. M. Guerrero, "Control design guidelines for single-phase grid-connected photovoltaic inverters with damped resonant harmonic compensators," *IEEE Trans. Ind. Electron.*, vol. 56, no. 11, pp. 4492–4501, Nov. 2009.

[17] R. Errouissi, H. Shareef, and A. Wahyudie, "A novel design of PR controller with antiwindup scheme for single-phase interconnected PV systems," *IEEE Trans. Ind. Appl.*, vol. 57, no. 5, pp. 5461–5475, Sep. 2021.

[18] J. Xia, Y. Guo, X. Zhang, J. Jatskevich, and N. Amiri, "Robust control strategy design for single-phase grid-connected converters under system perturbations," *IEEE Trans. Ind. Electron.*, vol. 66, no. 11, pp. 8892–8901, Nov. 2019.

[19] M. Mishra and V. N. Lal, "An advanced proportional multiresonant controller for enhanced harmonic compensation with power ripple mitigation of grid-integrated PV systems under distorted grid voltage conditions," *IEEE Trans. Ind. Appl.*, vol. 57, no. 5, pp. 5318–5331, Sep. 2021.

[20] H. Komurcugil, N. Altin, S. Ozdemir, and I. Sefa, "Lyapunov-function and proportional-resonant-based control strategy for single-phase grid-connected VSI with LCL filter," *IEEE Trans. Indus. Electron.*, vol. 63, no. 5, pp. 2838–2849, May 2016.

[21] X. Huang et al., "Robust current control of grid-tied inverters for renewable energy integration under non-ideal grid conditions," *IEEE Trans. Sustain. Energy*, vol. 11, no. 1, pp. 477–488, Jan. 2020.

[22] C. Meza, D. Biel, D. Jeltsema, and J. M. A. Scherpen, "Lyapunov-based control scheme for single-phase grid-connected PV central inverters," *IEEE Trans. Control Syst. Technol.*, vol. 20, no. 2, pp. 520–529, Mar. 2012.

[23] I. R. S. Priyamvada and S. Das, "Online assessment of transient stability of grid connected PV generator with DC link voltage and reactive power control," *IEEE Access*, vol. 8, pp. 220606–220619, 2020.

[24] D. Pan, X. Wang, F. Liu, and R. Shi, "Transient stability of voltage-source converters with grid-forming control: A design-oriented study," *IEEE J. Emerg. Sel. Topics Power Electron.*, vol. 8, no. 2, pp. 1019–1033, Jun. 2020.

[25] M. Reveles-Miranda, M. Flota-Banuelos, F. Chan-Puc, V. Ramirez-Rivera, and D. Pacheco-Catalan, "A hybrid control technique for harmonic elimination, power factor correction, and night operation of a grid-connected PV inverter," *IEEE J. Photovolt.*, vol. 10, no. 2, pp. 664–675, Mar. 2020.

[26] I. R. S. Priyamvada and S. Das, "Adaptive tuning of PV generator control to improve stability constrained power transfer capability limit," *IEEE Trans. Power Syst.*, vol. 37, no. 3, pp. 1770–1781, May 2022.

[27] S. Prakash, J. K. Singh, and R. K. Behera, "Lyapunov function based control strategy for single-phase grid-connected PV system with LCL-filter," in *Proc. IEEE Int. Conf. Power Electron., Drives Energy Syst. (PEDES)*, Dec. 2020, pp. 1–6.

[28] N. Beniwal, I. Hussain, and B. Singh, "Second-order volterra-filter-based control of a solar PV-DSTATCOM system to achieve Lyapunov's stability," *IEEE Trans. Ind. Appl.*, vol. 55, no. 1, pp. 670–679, Jan. 2019.

[29] S. Jayalath and M. Hanif, "Generalized LCL-filter design algorithm for grid-connected voltage-source inverter," *IEEE Trans. Ind. Electron.*, vol. 64, no. 3, pp. 1905–1915, Mar. 2017.

[30] T.-F. Wu, M. Misra, L.-C. Lin, and C.-W. Hsu, "An improved resonant frequency based systematic LCL filter design method for grid-connected inverter," *IEEE Trans. Ind. Electron.*, vol. 64, no. 8, pp. 6412–6421, Aug. 2017.

[31] P. E. Kakosimos, A. G. Kladas, and S. N. Manias, "Fast photovoltaic-system voltage- or current-oriented MPPT employing a predictive digital current-controlled converter," *IEEE Trans. Ind. Electron.*, vol. 60, no. 12, pp. 5673–5685, Dec. 2013.

[32] I. Poonahela, S. Bayhan, H. Abu-Rub, M. M. Begovic, and M. B. Shadmand, "An effective finite control set-model predictive control method for grid integrated solar PV," *IEEE Access*, vol. 9, pp. 144481–144492, 2021.

[33] M. A. Khan, A. Haque, V. S. B. Kurukuru, and S. Mekhilef, "Advanced control strategy with voltage sag classification for single-phase grid-connected photovoltaic system," *IEEE J. Emerg. Sel. Topics Ind. Electron.*, vol. 3, no. 2, pp. 258–269, Apr. 2022.

Surya Prakash (Graduate Student Member, IEEE) received the B.Tech. degree in electrical and electronics engineering from JNTUH Hyderabad, Hyderabad, India, in 2009, and the M.Tech. degree in power electronics engineering from VNIT Nagpur, Nagpur, Maharashtra, India, in 2012. He is currently pursuing the Ph.D. degree in electrical engineering with the Indian Institute of Technology (IITP), Patna, Bihar, India.

His research interests include control methods for power electronics converters in distribution systems and renewable energy resources, grid interconnection issues, power quality enhancement, and low-voltage ride-through.

Omar Al Zaabi (Member, IEEE) received the B.S., M.S., and Ph.D. degrees in electrical engineering from Pennsylvania State University, University Park, PA, USA, in 2012, 2014, and 2019, respectively.

He is currently an Assistant Professor with the Department of Electrical and Computer Engineering, Khalifa University, Abu Dhabi, United Arab Emirates. His current research interests include electromagnetic characterization and measurement techniques, target tracking and radar cross section (RCS) synthesis, and power electronics application.

Ranjan Kumar Behera (Senior Member, IEEE) received the B.Eng. degree in electrical engineering from the Regional Engineering College Rourkela, Rourkela, India, in 1998, and the M.Tech. and Ph.D. degrees in electrical engineering from the Indian Institute of Technology Kanpur, Kanpur, India, in 2003 and 2009, respectively.

Since 2009, he has been a Faculty Member and he is currently an Associate Professor with the Department of Electrical Engineering, Indian Institute of Technology Patna, Patna, India. His research interests include nonlinear control theory application to power electronic converters, pulsewidth modulation techniques, and multiphase electric drives control.

Dr. Behera was a recipient of the 2022 IEEE Outstanding Paper Award for IEEE TRANSACTIONS ON INDUSTRIAL ELECTRONICS.

Khaled Al Jaafari (Senior Member, IEEE) received the B.Sc. and M.Sc. degrees in electrical engineering (EE) from the Petroleum Institute, Abu Dhabi, United Arab Emirates, in 2006 and 2011, respectively, and the Ph.D. degree from the Department of Electrical and Computer Engineering, Texas A&M University, College Station, TX, USA, in 2016.

He has two years (2006–2008) of experience at ZADCO, Abu Dhabi, as an Electrical Engineer at the upper Zakum Oil field platform, where he was part of the site facility and maintenance engineering team. He is currently an Assistant Professor with the Khalifa University of Science and Technology, Abu Dhabi. His research interests include machines' condition monitoring, power system analysis, power system protection, and power quality studies.

Khalifa Al Hosani (Senior Member, IEEE) received the B.Sc. and M.Sc. degrees in electrical engineering from the University of Notre Dame, Notre Dame, IN, USA, in 2005 and 2007, respectively, and the Ph.D. degree in electrical and computer engineering from The Ohio State University, Columbus, OH, USA, in 2011.

He is currently an Associate Professor with the Department of Electrical and Computer Engineering, Khalifa University, Abu Dhabi, United Arab Emirates. He is the Co-Founder of the Power Electronics and Advanced Sustainable Energy Center Laboratory, ADNOC Research and Innovation Center, Abu Dhabi. His research interests include a wide range of topics including nonlinear control, sliding mode control, control of power electronics, power systems' stability and control, renewable energy systems' modeling and control, smart grid, microgrid and distributed generation, and application of control theory to oil and gas applications.

Utkal Ranjan Muduli (Senior Member, IEEE) received the B.Tech. degree in electrical and electronics engineering from the Biju Patnaik University of Technology, Rourkela, India, in 2011, the M.Tech. degree in electrical engineering from the Indian Institute of Technology Gandhinagar, Gandhinagar, India, in 2014, and the Ph.D. degree in electrical engineering from the Indian Institute of Technology Patna, Patna, India, in 2022.

He was a Visiting Scholar and a Research Associate with the Department of Electrical Engineering and Computer Science, Khalifa University, Abu Dhabi, United Arab Emirates, in 2019 and 2021, respectively, where he is currently a Post-Doctoral Research Fellow. His research interests include modulation strategies for multiphase motor drives, matrix converters and its control, battery power management, and wireless power transfer.

Dr. Muduli was a recipient of the 2022 IEEE Outstanding Paper Award for the IEEE TRANSACTIONS ON INDUSTRIAL ELECTRONICS.